Title: Liver regeneration by oval cells employing bistability of stemness-senescence, Hippo signaling, EMT-MET, and polyploidy circuit

Authors: Marija Lazovska[1,3] [*], Kristine Salmina[3], Dace Pjanova[2,3], Bogdan I. Gerashchenko[4] and Jekaterina Erenpreisa[3]

[1] Institute of Oncology and Molecular Genetics, Riga Stradins University, Riga, Latvia

[2] Riga Stradins University, Riga, Latvia

[3] Latvian Biomedical Research and Study Centre, Riga, Latvia

[4] R.E. Kavetsky Institute of Experimental Pathology, Oncology and Radiobiology, National Academy of Sciences of Ukraine, Kyiv, Ukraine; biger63@yahoo.com

[*] Corresponding author: Marija Lazovska, Institute of Oncology and Molecular Genetics, Riga Stradins University, Riga, Latvia, marija.lazovska@rsu.lv

Keywords

Liver regeneration; oval cells; bipotential progenitor; stemness-senescence; EMT-MET; polyploidy circuit; turbulence; replication stress; Hippo pathway

Abstract

Liver hepatocytes possess remarkable regenerative capabilities, yet severe damage may compromise this process. Liver progenitor ("oval") cells exhibit the potential to differentiate into both hepatocytes and cholangiocytes, making them promising candidates for cell therapy. However, their mechanisms in liver regeneration are not clear. Here, on rat liver oval stem-like epithelial cells (WB-F344) a wound healing assay was performed. The scratched near-confluent monolayers (70% area removed) underwent the G1-arrest, bi-nucleation at 10-12 hours post-wounding, starting movement of epithelial to mesenchymal transition (EMT) cell portion into the wounded areas. Nanog nuclear upregulation, fragmentation, and transition as granules into cytoplasm and around, along with $p16^{Ink4a}$ nuclear intrusion from the cytoplasm, loss of epithelial markers, and YAP1/Hippo activation were seen near the wound edge. The replicative stress and proliferation boost followed, documented at 24 hours. Proliferation concluded at 40-48 hours, accomplished by reconstitution of epithelial tissue, the disappearance of Nanog granulation and $p16^{Ink4a}$ return to the cytoplasm, releasing excess. This investigation reveals novel regulatory facets in liver regeneration by oval cells. It accentuates the stemness-senescence bistable switch regulated by reciprocal nucleo-cytoplasmic transitions of opposite regulators, coordinated with Hippo-pathway switch, replicative stress, and boost, along with ploidy, EMT-MET and paracrine secretome circuits - enabling successfully resolving the massive injury.

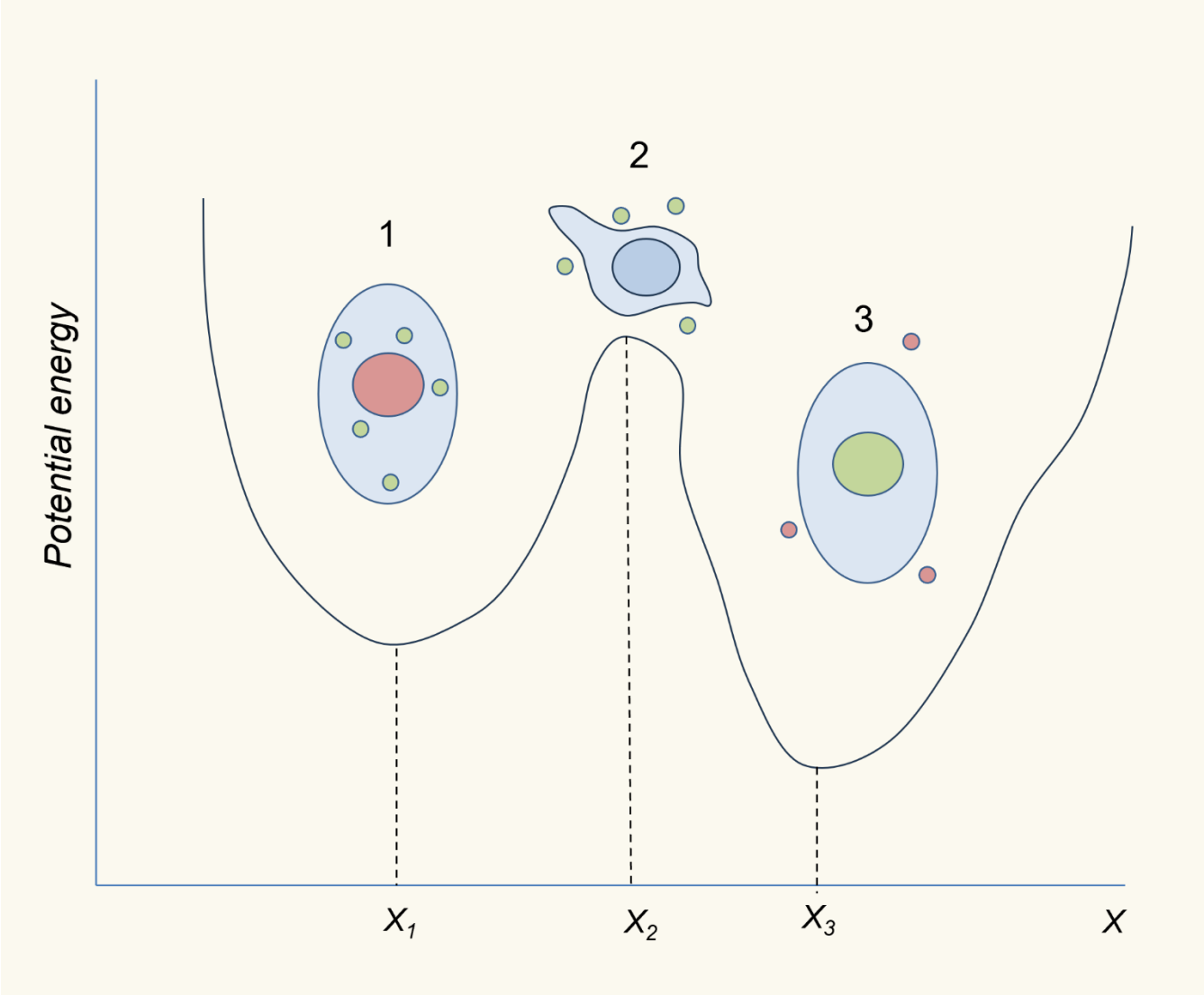

Fig 1. Graphical abstract. Bistable nuclear-cytoplasmic switch between stemness and senescence regulators in the wound healing process by oval liver cells: (1-2) Priming phase: (1) at the wound edge, (2) in the wound; (3) Proliferative phase, wound closure. Nanog – green; p16INK4A – red, EMT cell - with blue nucleus.

39 **Introduction**

40 The mammalian liver possesses a remarkable capacity to regenerate after the injury while recovering its
41 volume and functionality. However, the regenerative capacity of the liver is not endless: while the
42 removal of up to two-thirds of the liver (partial hepatectomy; PH) introduced in the experiment by
43 Higgins and Anderson in 1931 [1] can be safely repaired, larger resection is at risk of liver failure and
44 following the death of the patient. Unfortunately, there could be life-threatening situations due to
45 progressive complications of liver pathology that need to be eradicated as soon as possible by surgical
46 means. According to statistics, hepatic disease is one of the top causes of death globally and there is an
47 ascending tendency of diseases such as Hepatitis B and C often ending in cirrhosis and liver cancer [2].
48 At present, stem cell therapy is being extensively explored to tackle prognostically unfavorable liver
49 diseases [3]. Despite the progress, the challenges remain, and yet liver transplantation remains the only
50 curative treatment for patients with end-stage liver diseases.

51 Liver progenitor cells (LPCs)-driven liver regeneration was shown to be activated in case of massive liver
52 injuries (Duncan et al., 2009). It involves the activation and proliferation of the LPCs expressing
53 developmental markers and having the potential to become both mature hepatocytes and biliary cells
54 [4]. The events induced after the typical liver injury are usually categorized into three phases: priming
55 (activation), proliferation and termination [5]. Different signaling pathways and molecular processes are
56 involved, both LPCs- and hepatocyte-driven, also called typical liver regeneration performed by a healthy
57 liver. Many pathways are shared by both types of regeneration, but LPCs-driven repair remains less
58 understood. The Hippo pathway, one of the central growth regulators, was shown to accompany the
59 whole healing process from cell activation to the termination of response [6]. This pathway is involved
60 in replicative stress [7], and cellular polyploidy, which is described in normal liver and boosted by

61 regeneration [8, 9]. Senescence is another mechanism involved in liver repair; however, its role is
62 controversial and poorly understood [10, 11]. The unique hepatocyte plasticity and reprogramming to
63 an early postnatal-like state in response to injury were shown using a single-cell RNA sequencing [12].

64 In this work, using an *in vitro* wound healing assay, we study rat LPCs (known as "oval" epithelial cells)
65 in response to mechanical injury. The primary goal of the study is to find out how the previously
66 described mechanisms are interconnected in time and space by combining phenotypical and molecular
67 studies of LPCs throughout the healing process. Here, in addition to the already known "polyploidy
68 circuit", in which polyploid hepatocytes undergo ploidy reduction during injury response and subsequent
69 re-polyploidization [13] together with Hippo pathway on-off state, we describe cooperation and
70 "competition" between the opposite regulators of cell fate - senescence/quiescence and stemness/self-
71 renewal. Replicative stress, which is likely imposed by YAP1 in this wound healing assay, could be a key
72 contributor in this bistability directed towards the regulation of cell-fate changes.

73 **Methods**

74 **The cell line**

75 The non-transformed male diploid WB-F344 rat liver epithelial cell line [14] was kindly provided by Dr.
76 Tomonori Hayashi (Radiation Effects Research Foundation, Hiroshima, Japan). It is a benign wild-type
77 p53 stem-like cell line, rapidly proliferating, and potentially capable of differentiating into both
78 hepatocytes and cholangiocytes. In addition, these cells are relatively radioresistant as they do not
79 undergo rapid and massive cell death even after high-dose irradiation up to 10 Gy [15]. The cells were
80 cultured in RPMI 1640 growth medium (Sigma-Aldrich, St. Louis, MO, USA) supplemented with 7% fetal
81 bovine serum (FBS) (Sigma-Aldrich, St. Louis, MO, USA) and 600 µg/ml L-glutamine (Gibco; Thermo Fisher

82 Scientific, Waltham, MA, USA). Cells were incubated at 37°C in a humidified 5% CO2 atmosphere with
83 complete medium replacement performed every 24 h. Cells were routinely subcultured after reaching
84 70-80% confluency every three days.

85 **Wound healing (scratch) assay**

86 Before wound healing assay, cells were grown on 4-well glass chamber slides coated with poly-D-lysine
87 (Thermo Fisher Scientific, Waltham, MA, USA). About 70,000 cells were seeded in each chamber well
88 with a total aliquot of growth medium of 1 ml. To mimic the organ regeneration after the wounding and
89 to test the wound-induced plasticity of WB-F344 cells, a simple wound healing (scratch) assay was
90 applied. For this purpose, cell monolayers that were maintained in chamber slides reaching the near-
91 confluence of approximately 95% after 24–30 h culturing were used. A sterile 1000 µl pipette tip was
92 used to scratch a grid composed of longitudinal and transverse lines (approximately 9 and 6 lines,
93 respectively), so the distance between the closest non-intersecting lines was almost equal (~ 2 mm).
94 Approximately two-thirds of the monolayer was removed. To take away cell debris, the cell monolayers
95 were washed three times with pre-warmed culture media by gentle shaking followed by the addition of
96 fresh media. Cells were then incubated at the aforementioned conditions until the desired time point or
97 full closure of the wound. An Experimental design of the wound healing assay is shown in Fig 2.

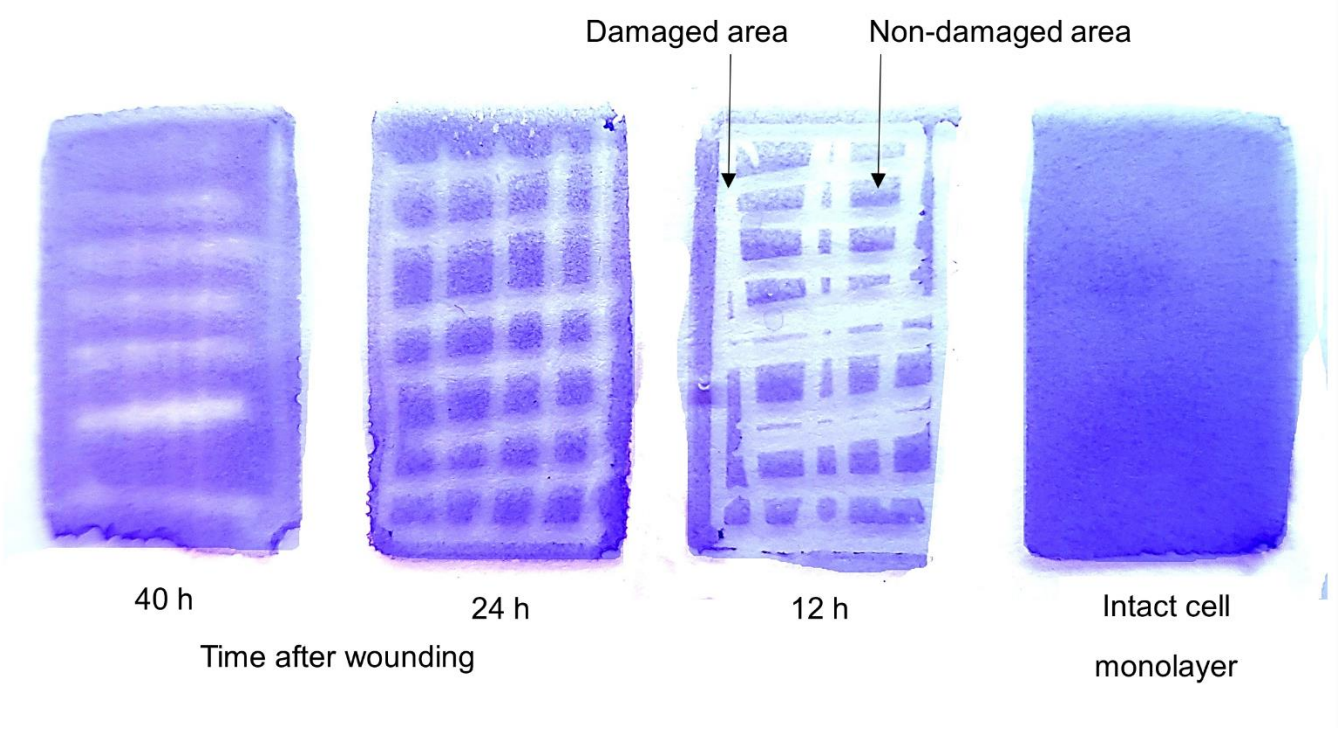

Fig 2. Experimental design. Monolayers of WB-F344 cells after reaching near 100% confluence in chamber slides were scratched and at 40, 24, and 12 h after wounding were fixed and stained with Toluidine blue (TB) for analysis. The highlighted enlarged region of interest from one of the TB-stained monolayers demonstrates different densities of cells in damaged (scratched) and non-damaged (non-scratched) areas colored in white and blue, respectively. Based on spatial localization to wound the edge the cells were subsequently analyzed for DNA content by image cytometry and cell-cycle phase-dependent nuclear morphology.

Immunofluorescence staining

For immunofluorescence staining the chamber slides with live scratched adherent cells were removed from growth media and rinsed three times with warm phosphate-buffered saline (PBS), pH=7.4 (Sigma-Aldrich, St. Louis, MO, USA), and afterwards a droplet of warm FBS was added to each well. Before the next manipulations, a chamber was gently pulled off from the slide and the slides were allowed to shortly

111 air-dry vertically. Then cells were fixed in methanol for 7 min at -200C, dipped 10 times in ice-cold
112 acetone, and allowed to briefly dry. Slides were washed three times in 0.01% tris-buffered saline/Tween
113 20 (TBST) for 5 min each. Subsequently, they were blocked for 40 min in 1% bovine serum albumin (BSA)
114 in PBS with 0.05% Tween-20 (Sigma-Aldrich, St. Louis, MO, USA) at room temperature (RT). After
115 blocking, the samples were covered with 1% BSA in PBS with 0.025% Tween-20 containing primary
116 antibodies and incubated overnight at 40°C in a humidified chamber. The next day, slides were washed
117 five times in 0.01% TBST and covered with TBST containing appropriate secondary antibody in 1:300
118 dilution (goat anti-mouse IgG Alexa Fluor 488, goat anti-rabbit IgG Alexa Fluor 594 (Invitrogen, Carlsbad,
119 CA, USA)) and incubated for 40 min at RT in the dark in a humidified chamber. After incubation, the
120 samples were washed again five times with 0.01% TBST and once for 2 min in 1xPBS. Cells were
121 counterstained with DAPI (0.25 µg/ml) for 2 min and embedded in Prolong Gold (Invitrogen, Carlsbad,
122 CA, USA). When staining for α-tubulin and actin, the cells were fixed with fresh warm (~ 37°C) 4%
123 paraformaldehyde for 15 min at RT, then washed three times with 1xPBS and permeabilized with 0.5 %
124 Triton-X100 (Sigma-Aldrich, St. Louis, MO, USA) in 1xPBS for another 5 min, washed again; and further
125 the previously described steps starting from blocking were carried out. Three independent experiments
126 for each combination of primary antibodies were performed. For microscopic observations and sample
127 analysis, a fluorescent light microscope (Leitz Ergolux L03-10, Leica, Wetzlar, Germany) equipped with a
128 color video camera (Sony DXC 390P, Sony, Tokyo, Japan) and RGB filter-set were used. Primary
129 antibodies and their sources are listed in Table 1.

130 **Table 1. List of antibodies used in this study for immunofluorescence staining.**

Antibody Against	Description	Used concentration	Product no. and Manufacturer

α-Tubulin	Mouse monoclonal	1:200	T5168, Sigma-Aldrich, St. Louis, MO, USA
Albumin	Rabbit polyclonal	1:200	PA5-85166, Invitrogen, Carlsbad, CA, USA
Nanog	Mouse monoclonal	1:50	N3038, Sigma-Aldrich, St. Louis, MO, USA
Twist1	Mouse monoclonal	1:100	sc-81417, Santa Cruz, Dallas, TX, USA
Cytokeratin 7	Mouse monoclonal	1:100	MA1-06315. Invitrogen, Carlsbad, CA, USA
Oct 3/4	Mouse monoclonal	1:40	sc-5279, Santa Cruz, Dallas, TX, USA
p16^{Ink4a}	Rabbit polyclonal	1:50	ab84075, Abcam, Cambridge, UK
TEAD1	Mouse monoclonal	1:200	GT13112, Invitrogen, Carlsbad, CA, USA
F-ACTIN	Phalloidin-iFlour 594 Conjugate	1:300	ab176757, Abcam, Cambridge, UK
YAP1	Rabbit polyclonal	1:500	PA-46189, Invitrogen, Carlsbad, CA, USA

c-Myc	Mouse monoclonal	1:100	sc-40, Santa Cruz, Dallas, TX, USA

131 **DNA staining and image cytometry**

132 To evaluate DNA amount in cells, count mitotic figures and estimate cell cycle dynamics the samples
133 were stained with toluidine blue (TB) by the method [16], by the following protocol. Chamber slides with
134 adherent scratched or control cells were washed three times with 1xPBS as described before, with
135 subsequent addition of warm FBS and air-drying for 30 min. Then slides were fixed in ethanol/acetone
136 (1:1) for at least 30 min at 40°C and then air-dried again. Next, slides were hydrolyzed with 5 N HCl for
137 20 min at 20-21°C. In some experiments, to partly preserve RNA staining and observe nuclei together
138 with the cytoplasm, a shortened hydrolysis for 10 sec was performed. Slides were then washed in
139 distilled water five times 1 min each and stained with 0.05% TB in 50% citrate-phosphate McIlvain buffer
140 at pH=4 for 10 min. They were briefly rinsed in distilled water and blotted with filter paper. Subsequently,
141 the slides were dehydrated by incubating twice in butanol for 3 min each at 37°C, cleared twice in xylene
142 for 3 min each at RT and embedded in DPX. Ready samples were imaged in the green channel using a
143 Sony DXC 390P color-calibrated video camera (Sony, Tokyo, Japan). From the greyscale images, DNA
144 content was measured as the IOD using Image-Pro Plus 4.1 software (Media Cybernetics, Rockville, MD,
145 USA). Cell DNA content or ploidy number was compared to IOD values for metaphases and anaphase-
146 telophase (ratio= 2) and equated to diploid (2C) DNA values in G1 cells. A sum error of 10% was
147 established for this DNA stoichiometry method using in situ image analysis, and this interval was
148 considered for estimating proportional distribution of cell-cycle phases. For cell cycle measurements,
149 approximately 300-500 interphase cells were collected at each experimental time point. Mitotic indexes

150 were measured microscopically per 1000 cells, as well as other characteristics, such as the number of
151 binuclear cells.

152 **Statistical analysis**

153 Statistical analysis was performed with the Student's t-test tool on Microsoft Office Excel (version 2401).
154 Statistical significance was assessed at a p-value < 0.05.

155 **Results**

156 **Cell growth arrest and polyploidy/cell cycle changes at the wound edge – the early response**

157 In control cells, the cell cycle exhibited a standard distribution, with most cells progressing smoothly
158 through the G1 phase (diploid fraction) (Fig 3B and 3E). G2 and S phases were well-represented,
159 indicating normal cell cycle progression. Upon injury, a notable shift occurred in cell cycle dynamics at
160 12 hours post-injury (hpi). Most cells exhibited arrest at the G1 phase, accompanied by a reduction in
161 G2 and S phases, in stark contrast to the control (Fig 3B). Interestingly, the mononuclear polyploid cell
162 (>4C) fraction significantly decreased from 3.88% to 0.95% (Fig 3E and 3F), while the proportion of
163 binuclear cells tripled from 1% to 3%, with a higher accumulation at the wound edges (about 5%) (Fig
164 3D). This indicated the activation of a polyploidy circuit in response to the wound. Concomitant with
165 considerable G1 phase arrest, the proportion of mitotic cells decreased twofold compared to control
166 (from 1.45% to 0.65%) (Fig 3A) at the wound edge. At the same time, there was a fourfold increase in
167 the anaphase+telophase/metaphase ratio (from 1.3 to 5.2) (Fig 3C), highlighting a substantial
168 acceleration of divisions in some small proportion of cells. This early response within the first 12 hours
169 post-injury suggests a complex interplay of cell cycle regulation in reaction to tissue damage.

170

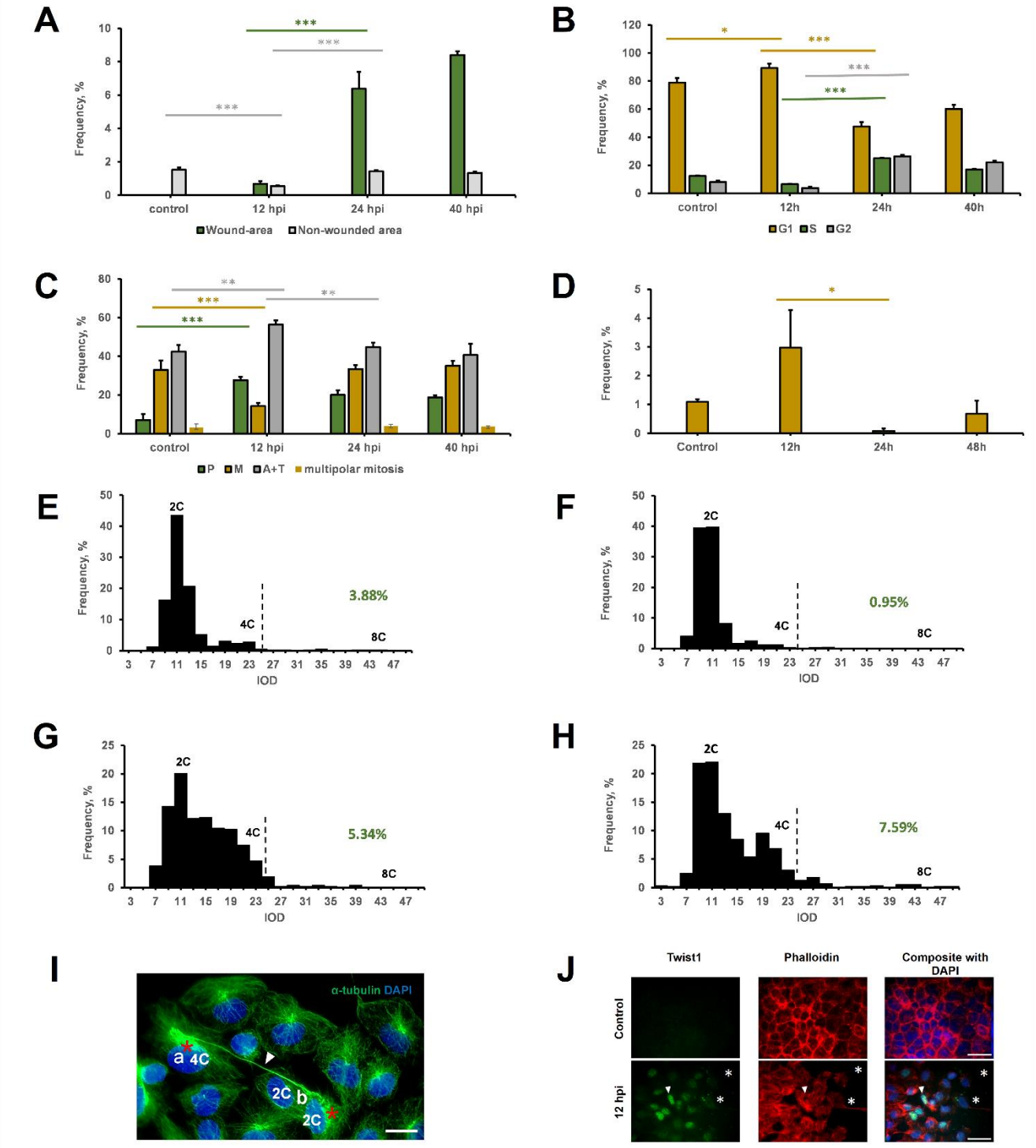

171

172 **Fig 3. Post-wounding effects on nuclear morphology quantitative data (A-D), DNA content profiles (E-**

173 **H) and immunofluorescence characteristics of α-tubulin (I) and Twist1 (J) of WB-F344 cells.** (A) Mitotic

174 indexes at different time points after wounding were separately counted within scratched and non-
175 scratched areas. (B) Distributions of mitosis stages of cells at the edge of the wound at different time
176 points after wounding. (C) Distributions of cell-cycle phases (G1, S, and G2) of cells at the edge of the
177 wound at different time points after wounding. (D) Fraction of binucleated cells at the edge of the wound
178 at different time points after wounding. Data presented as a mean ± SE from three independent
179 experiments. ****: $p \leq 0.0001$, ***: $p \leq 0.001$; **: $p \leq 0.01$, *: $p \leq 0.05$, ns: $p > 0.05$. Representative cell-
180 cycle phase distributions by in situ DNA cytometry in control (E) and within the wound edge/gap at 12 h
181 (F), 24 h (G) and 40 h (H) after wounding. The integral optical density (IOD) values shown in arbitrary
182 units correspond to the positioning of DNA content per cell nucleus. The dashed lines represent borders
183 separating cell nuclei exceeding 4C DNA ploidy whose percentages are shown in green. (I) Cells at the
184 wound edge stained for α-tubulin (green) and DNA by DAPI (blue) display two tetraploid daughter cells
185 ("a" and "b") whose centrosomes (shown by black asterisks) are still joined by a long bridge (shown by
186 white solid arrowhead), which is indicative of the relatively recent cytokinesis that took place a few hours
187 ago; however, the daughter cell "b" has already managed to perform an apparent karyokinesis, thus
188 forming a binuclear (2C+2C) cell, whereas the daughter cell "a" remains quiescent. (J) There is no Twist1
189 expression in control (intact cells) with a typical "cobblestone" epithelial pattern of actin staining (red),
190 whereas Twist1 (green) is highly expressed in cell nuclei within the wound edge especially at 12 h after
191 wounding. Here the wound gap is shown by asterisks, and at the wound edge some cells with reorganized
192 actin cytoskeleton have extending lamellipodia (shown by arrowhead). Scale bars = 10 µm (I) and 30 µm
193 (J).

194 **Interplay of the opposite senescence and stemness regulators at the early priming phase**

195 In the absence of injury, control cells displayed a low-level presence of the senescence marker and
196 Cdk4/6 inhibitor p16^{Ink4a} in cell-nuclei and cytoplasm, suggesting some intrinsic balanced activity (Fig 4A).
197 Concomitantly, the stemness regulator Nanog exhibited a moderate nuclear presence in control cells
198 (Fig 4A). This baseline expression of Nanog in the absence of injury underscores its role as a master
199 regulator of stemness in oval cells even under normal conditions. Upon initiation of the early priming
200 phase following injury, both p16^{Ink4a} and Nanog displayed increased presence in cell nuclei, as evidenced
201 by comparative immunofluorescence images. Moreover, while in control of confluent cultures a few
202 Nanog granules were encountered in the cytoplasm, their abundance appeared in the cytoplasm and
203 interspersed among cells at the wounded edge at 10-12h (Fig 4B). Interestingly, cells rich in cytoplasmic
204 Nanog granules exhibited weaker nuclear staining for Nanog but stronger staining for p16^{Ink4a} compared
205 to cells with fewer cytoplasmic granules (Fig 4B, arrowed). This observation hints at the dynamic
206 interplay between these regulators and the potential influence of their subcellular localization on the
207 cell's fate. Another stemness and stress-related transcription factor and an immediate early gene
208 response in liver regeneration, Myc was also of interest. While mostly background cytoplasm Myc-
209 staining was seen in control WB-F344 cells (Fig 4E), at 12 hpi, at the wound edge cells, this was
210 particularly concentrated at the centrosome area and outlined the cytoskeleton (Fig 4F), likely being
211 presented by MycN. Its overexpression is known as arresting the centrosome cycle after DNA damage,
212 in cooperation with wild type p53 [17]. However, the absence of Myc in cell nuclei testified to its
213 suppressed activity as a transcription factor, in line with the decreased nuclear location of Nanog when
214 overcompeted by cytoplasmic-nuclear p16^{Ink4a} influx. At the same time, this resulted in the Nanog
215 protein displacement into cytoplasm as granules and conditioning of the microenvironment at a

216 wounded edge with the stemness-self-renewal factor, which could paracrinally and autocrinally boost

217 the next, proliferating phase of wound healing.

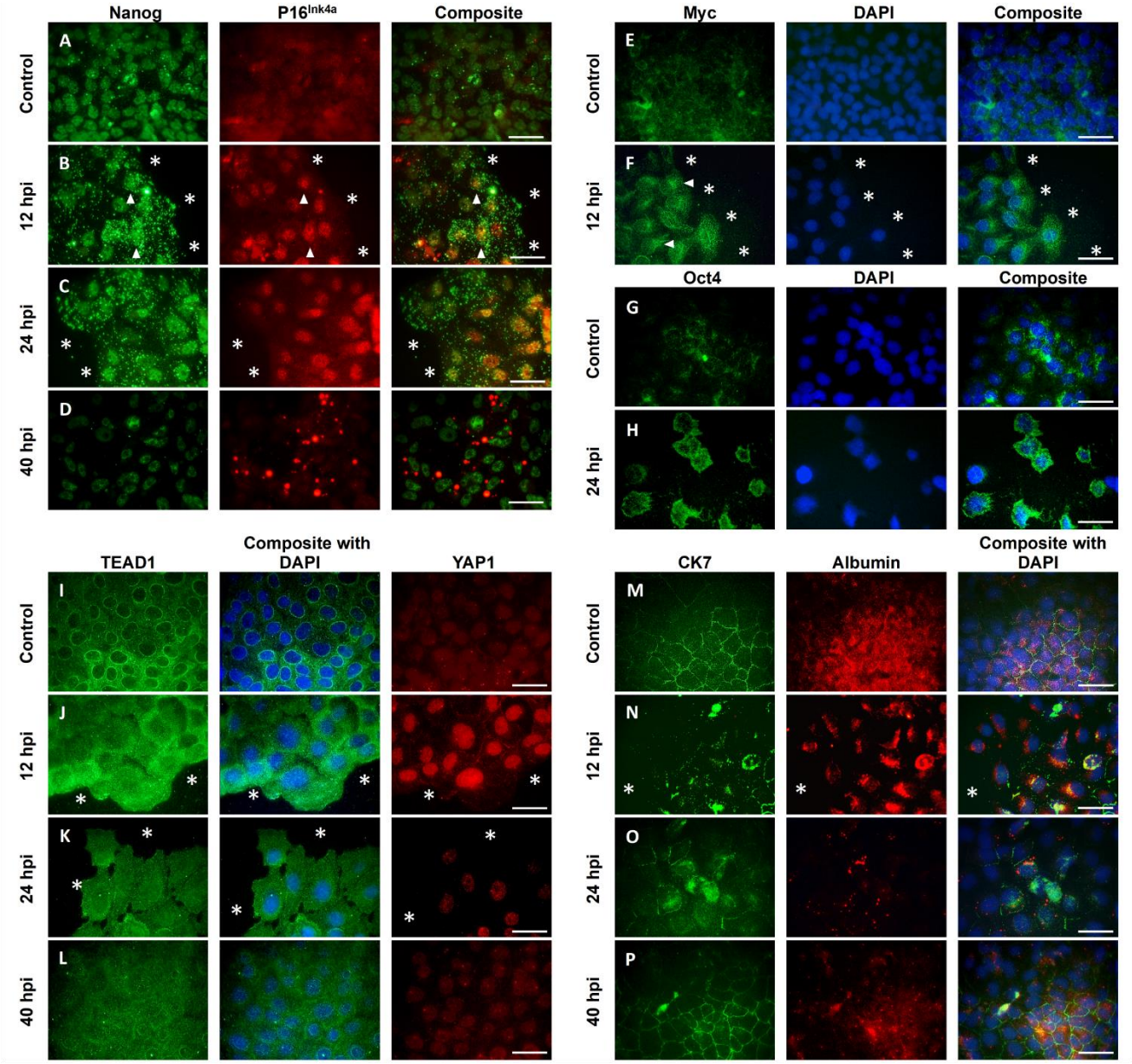

218

219 **Fig 4. Post-wounding effects on localization, expression, and dimensional characteristics of**

220 **immunofluorescence of Nanog and p16^{Ink4a} (A-D), Myc counterstained with DAPI (E-F), TEAD1 and**

221 **YAP1 counterstained with DAPI (I-L), and CK7 and albumin counterstained with DAPI (M-P)**. Notably,

222 at 12 h after wounding, there is an increase of Nanog cytoplasmic granules (size and numbers)
223 accompanied by an increase of p16^{Ink14a} nuclear expression, as the white arrowheads show some most
224 representative cases (B). In contrast, at 40 h after wounding, many variously sized 16^{Ink4a} granules
225 drastically appear in the cytoplasm with the disappearance of Nanog cytoplasmic granules (D). At the
226 same time, Myc at 12 h after wounding (F), compared with the control (E) increases in the cytoplasm,
227 especially in the centrosome area (white arrowhead) of cells located closer to the wound edge. Also, at
228 the wound edge, cells have an increased cytoplasmic Oct4 (H), compared to the control cells that express
229 Oct4 in cytoplasm as well as in nuclei to an insignificant extent representing background levels (G).
230 Differently localized YAP1 and TEAD1 are well expressed over an active wound healing process (J and K),
231 pointing out the fact that after wounding (especially at 12 h; J) TEAD1 becomes markedly expressed in
232 nuclei and cytoplasm of edge cells, and these cells are also characterized by an elevated and distinct
233 nuclear YAP1 expression. However, these peculiarities diminish upon the wound closure time (L).
234 Contrary to cells actively involved in wound healing, control cells have well-defined nucleo-cytoplasmic
235 TEAD1 rings and dimly stained nuclear YAP1 (I). Albumin and CK7 drastically and synchronously change
236 throughout wound healing (N, O, and P). Although there is an apparent difference in their localization,
237 some shared patterns of colocalization may also be present. Further explanations are in the text.
238 Asterisks (*) indicate the wound gap. Scale bars = 30 µm.

239 The change in cell ploidy and fate, motivated us to look at the Hippo pathway, an important cell and
240 tissue growth regulator, in particular its main operators – transcription regulator YAP1 and its binding
241 target in the nucleus, transcription factor TEAD1. Under basal conditions, control cells displayed YAP1
242 and TEAD1 subdued intensity and were notably absent in nuclei, as depicted in Fig 4I. Interestingly,
243 TEAD1 revealed ring-like structures at the inner perimeter of the nuclear envelope (Fig 4I), potentially

244 signifying lamin B1 rotation associated with accelerated cell senescence, which may be an indirect sign
245 of the lamin B1 rotation in accelerated cell senescence and of cell nucleus turbulence observed preceding
246 YAP1 activation [18]. As the early wound response developed, a notable reconfiguration in the Hippo
247 pathway dynamics became apparent. At 12 hpi, cells at the wound edge exhibited increased YAP1
248 nuclear staining, coupled with an overall increase in TEAD1 (Fig 4J). This heightened activation indicated
249 a responsive modulation of the Hippo pathway, implicating it in the cellular and tissue growth regulation
250 triggered by the injury. The initial wound response also induced substantial alterations in cell phenotype,
251 characterized by the loss of epithelial markers (CK7 and albumin), disorganization of the cobblestone-
252 like tissue structure, and reorganization of the actin cytoskeleton (Fig 4N and 4O). Additionally, the
253 emergence of lamellipodia (Fig 3J, arrowed) indicated a shift toward a mesenchymal phenotype,
254 suggestive of an EMT process.

255 Twist1, a pivotal transcription factor associated with EMT initiation, displayed intense nuclear staining
256 within wound edge cells at 12 hpi, in stark contrast to its absence in control cells (Fig 3J). This observation
257 provided further substantiation for the occurrence of EMT during the initial phases of the wound
258 response.

259 **Proliferation burst, MET and Nanog/p16^{Ink4a} interplay resolution as the late wound response of WB-**
260 **F344 cells.**

261 At 24 hpi there starts a tremendous elevation of mitotic activity, which continues to grow at 40 hpi (Fig
262 3A), 4- and 5-fold increasing mitotic index, respectively, compared with control. The proportions of
263 metaphases and anaphase+telophase phases at these time points were comparable with the control,
264 approximately 1.1 - 1.3 (Fig 3C). In cell cycle histograms, at 24 hpi instead of one peak at 2C and another
265 at 4C, we found a “ladder”- like histogram starting from G1, embracing a very bulk S-fraction fusing with

266 G2 and extending up to the hyper-tetraploid fraction (Fig 3G). More conventional histogram was
267 obtained at 40 hpi within the cells in the damaged area with peaks at 2C and 4C, however, some “ladder”
268 remnants could be seen (Fig 3H); the polyploidy (mononuclear) level continued to increase from 24 hpi
269 and was 1.5-fold higher in comparison with control, also octoploid and even bigger ploidy cells are
270 already seen (Fig 3E-3H). Dropped to about 0.2% at 24 hpi (Fig 3D) the frequency of binuclear cells may
271 indicate their attraction to the wound, followed by segregation and use in the wound healing process
272 occurring before the burst of mitosis.

273 At the time of proliferation burst (24 and 40 hpi) WB-F344 cells regained epithelial phenotype (Fig 4O
274 and 4P), no expression of Twist1 is present anymore (data not shown) and YAP1 and TEAD1 staining
275 became less intense, suggesting Hippo pathway tumor suppressing function resuming (Fig 4K and 4L).
276 Interestingly, we found that Oct4, one of the main stemness factors, while weakly stained with the
277 monoclonal antibody (covering the 1st exon) in control WB-F344 cells (Fig 4G), and at 24 hpi show the
278 non-specific antibody binding exclusively within morphologically distinct, distorted nuclei. The absence
279 of the nuclear Oct4 staining in our model indicates the absence of the nuclear binding and hence the
280 transactivating activity, in line with the absence of C-Myc activity in cell nuclei (Fig 4E and 4F) and may
281 also indicate to the restricted p53-controlled stemness potential of oval cells. The interplay between two
282 opposites for cell fate proteins, self-renewing Nanog or senescence-inducing $p16^{INK4A}$ continue to show
283 heterogeneous patterns (presuming oscillations) at 24 hpi at the wound edge started early after the
284 injury (Fig 4C), however, resolution comes at 40 hpi (almost full wound closure time) when Nanog over-
285 dominated and “casted-out” $p16^{Ink4a}$ from cell nuclei (Fig 4D). Previously rich in Nanog granules, cellular
286 cytoplasm is now clear from them, however, differently sized $p16^{Ink4a}$ positive cytoplasmic granules and
287 aggregates, approximately 1-3 per cell (if present) appeared (Fig 4D). It could be deduced, the “bistable

288 switch" between two toggles – stemness and senescence – in WB-F344 cells occurring along with wound

289 healing phases provides its positive outcome.

290 A summary of the observed cell changes during the whole wound healing process is provided in Table 2.

291 **Table 2. Summary of the observed events during the *in vitro* regeneration model.**

Cellular characteristics	Marker	Localization	Time points			
			Control	12hpi	24hpi	40hpi
Stemness	Nanog	Nucleus	+	++	++	+
		Cytoplasm	+/- few granules	++ granules	++ granules	+/-
Senescence	$P16^{Ink4a}$	Nucleus	+	++	++	-
		Cytoplasm	+ diffuse	++	++	+ granules
Bi-potential tissue-specific stemness potency	Albumin (hepatocyte)	++ diffuse	+/-	+/-	+	Albumin (hepatocyte)
	Cdk7 (cholangiocyte)	++	+/-	+/-	++	
Mobility EMT	Twist1		-	++	-	-
	Phenotype		Epithelial phenotype	EMT	EMT	MET
Hippo pathway	YAP1	Nucleus	+/-	+++	++	+
		Cytoplasm	+/-	-	-	-
	TEAD1	Nucleus	- peri-nuclear rings	+	+	+
		Cytoplasm	+	++	+	+

292 Outlined is the dynamic behavior of various cellular markers associated with key biological processes

293 such as Stemness, Senescence, Bi-potential tissue-specific stemness potency, Mobility, and Hippo

294 pathway over distinct time points post-injury (hpi) (12, 24, and 40 hours). Each row corresponds to a

295 specific cellular characteristic, detailing the behavior of distinct markers and their localization within the
296 cell. The markers exhibit diverse patterns of localization (nucleus, cytoplasm), intensity (+, ++, - or +/-)
297 indicative of their presence or activity, and distinctive cellular behaviors (e.g., granules, diffuse,
298 transition states like EMT and MET).

299 **Discussion**

300 Activation of the liver oval cells that contribute to liver regeneration is commonly observed in chronic or
301 severe (acute) liver injury [19]. Diverse paracrine and autocrine signaling pathways have been described
302 to control the LPC response [20]. However, it is far from being clear regarding the mechanisms that can
303 be involved *in vivo* and *in vitro* systems for successful liver regeneration, especially in case of serious
304 pathology. There is also an important concern about the therapy by LPCs in terms of its oncological
305 safety. In the current study, we induced the massive injury, mechanically removing ~70% of the culture
306 monolayer of rat liver oval cells. In general, two phases of cell response to injury ("priming" and
307 "proliferation") were observed, which is in accord with the findings from *in vivo* models of partial
308 hepatectomy [5]. Moreover, cell ploidy changes during the healing process including transient
309 binucleation were also demonstrated, confirming the findings previously reported [13]. However, for the
310 first time we were able to reveal and monitor the regulation of wound healing by the progenitor-driven
311 liver regeneration involving the recurrent nucleo-cytoplasmic transfer of two opposite regulators, Nanog
312 (stemness/cell-cycle progression) and $p16^{Ink4a}$ (senescence/cell-cycle arrest). The upregulation of Nanog
313 at the priming stage (10-12 hp) was converted into Nanog secretion in the form of cytoplasmic and
314 extracellular Nanog-positive granules (vesicles) being outcompeted for the nuclear binding sites by
315 $p16^{Ink4a}$ transferred into cell nuclei from cytoplasm. Both regulators are known to compete for the same
316 Cdk4/6 kinase of Cyclin D controlling the G1/S cell cycle checkpoint in stem cells: Nanog as an activator,

317 whereas p16^{Ink4a} as an inhibitor [21, 22]. Upon completion of cell proliferation at 40-48 h post-wounding,
318 the backward process is taking place: Nanog ousts p16^{Ink4a} from cell nucleus binding sites to cytoplasm,
319 suppressing the excited dual state of accelerated cell senescence, which was induced by the damage.
320 Thus, this system can be adapted to severe damage by employing a bistable switch of self-organization
321 (schematically shown in the Graphical abstract). At present, the concept of bistable switch-based
322 regulation is well-recognized and being intensively developed by Systems Biology as an example of
323 adaptive thermodynamics applicable to stem, differentiated and tumor cells [23-28]. In some previous
324 studies with breast tumor cells, there were possible fluctuations of cells with accelerated senescence
325 induced by drugs, e.g., between the Nanog- and p16-positive, including intermediate states [26, 29].
326 Moreover, the experiments with knockout mice showed that senescence, in particular, its p16^{Ink4a}
327 regulator is not only an antagonist of stemness but also is indispensable (along with secreted Il-6) to
328 promote reprogramming [30, 31]. Although usually this feature is solely ascribed to the senescence
329 secretome, here we demonstrate that the relationship between the potentially reprogramming Nanog
330 and senescing p16^{Ink4a} regulators is more complex with the involvement of nucleo-cytoplasmic relocation
331 of these two opposites, resulting in the negative feedback during second phase ending the healing
332 process. The reprogramming potential of the epithelial oval cells (WB-F344) used in this study was also
333 displayed by EMT-MET dynamics (as part of the same bistable switch), suggesting biphasic character of
334 also this process. The Hippo pathway, which is known to be associated with changes of cell fate and
335 ploidy [32, 33], has been also described in the context of liver regeneration and development [6]. We
336 found the Hippo pathway inactive in the near-confluent WB-F344 cell culture but it can be activated by
337 turbulence (as judged by perinuclear rings of TEAD1) and cytoplasmic-nuclear transition of activated
338 YAP1 that coincides with the priming phase and continues during replicative stress preceding and

339 accompanying the boost of proliferation at 24 h. The proliferation-associated “staircase” form of DNA
340 histograms starting from the early S-phase can be suggestive of the “staggering” of replication forks
341 caused by transcription R-loops [34]. This phenomenon is ascribed to hypertranscription activity of
342 nuclear YAP1 that functions in partnership with TEAD1 [35].

343 In fact, the WB-F344 line can be referred to as somatic oval cells possessing stem-like features, such as
344 an asymmetric cell division producing the progeny of different fates (differentiation and self-renewal).
345 Stem cells usually reside in quiescence and proliferate under stimuli [36]. However, cell-cycle regulation
346 of adult stem cells has not been explored as much as that of embryonic stem cells (ESCs). Most distinct
347 features of the cell-cycle of ESCs are as follows: non-functional G1/S-checkpoint, allowing rapid
348 proliferation, low functionality of the S-checkpoint, while the G2/M-checkpoints and spindle becomes
349 uncoupled from apoptosis [37, 38], favoring mitotic slippage into polyploidy.

350 In our model, DNA histograms of the near-confluent intact control showed most quiescent cells with low
351 mitotic index (MI) and insignificant degree of polyploidy (>4C). At the same time, there were cell-cycle
352 progression delay at 12 hpi with a halved mitotic index accompanied by disappearance of mononuclear
353 polyploid (>4-8C) cells and increasing of diploid (G0/G1) fraction with a negligible level of S-phase cells.
354 Notably, at 24 hpi there was a 5-fold but moderate elevation of polyploid fraction (>4C), not exceeding
355 8%. That means that the G1/S-checkpoint became adapted, thereby resulting in cell-cycle acceleration,
356 although S-phase was “staggering” at stalling replication forks due to collision between enforced
357 replication and hyper-transcription of active genes at the beginning of S-phase [39], which is suggestive
358 of replicative stress. In this situation, the “leakage” of the adapted G2/M-checkpoint with a lowered
359 threshold may reduce this stress, diverting a proportion of replicated cells from the mitotic cycle into
360 polyploidy (4C-8C). Our counts show a clear reciprocal relationship between the numbers of bi-nucleated

361 and mononucleated polyploid cells. One could suggest that those may be playing a role of the reservoir
362 for the emergent adaptation to wounding, thereby initially saving the energy needed for new DNA
363 synthesis. Therefore, it seems logical to hypothesize that only these types of cells (binucleated and
364 mononuclear polyploids) acquire the plasticity-assigned features of “avant-garde” undergoing EMT,
365 which is necessary for initial loose filling of the wound gap creating the stromal substrate for the
366 upcoming proliferation, simultaneously boosted by the Nanog-containing secretome. Once the
367 aforementioned priming response is completed and binucleate cell pool becomes exhausted, the energy
368 of mitosis due to the renewed DNA synthesis is directed to the formation of the next stock of polyploid
369 cells (the hypothetical Scheme of the ploidy response in oval cells using the binucleation/polyploidy (2C-
370 4C-8C) conveyor is presented in Fig 5.

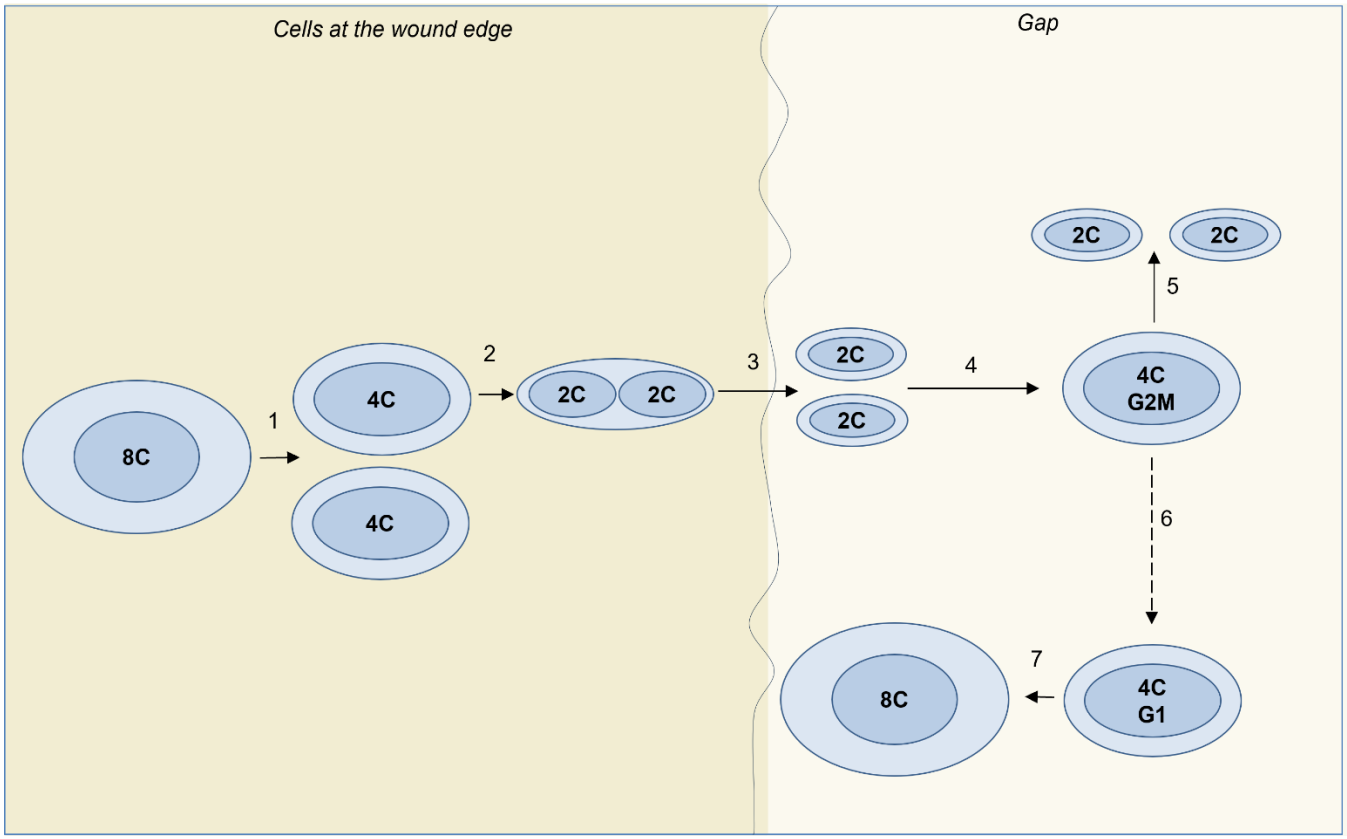

371

372 **Fig 5. Hypothesis: Oval cells' ploidy circuit in wound healing.** (1) After the injury the fraction of polyploid
373 8C cells undergoes reductive divisions resulting in 4C cells, which (2) immediately perform cytokinesis-
374 deficient karyokinesis producing binucleate cells. (3) 4C binucleate cells undergo postponed reductive
375 cytokinesis, producing 2C daughters moving into the wound gap as mesenchymal cells via EMT. (4) In
376 the wound gap, cells regain epithelial phenotype via MET and enter the mitotic cycle to replenish the
377 pool of 2C cells (5). However, a portion of cells via mitotic slippage (6) advance to the new polyploidy
378 cycle, restoring an exhausted pool of polyploid cells (7).

379 It is important to stress that this two-way process can be well organized by the negative feedback, thus
380 restricting the potential of uncontrolled growth that would let the "tumor genie out of the bottle". All
381 toggles observed here, such as Nanog/p16, EMT/MET, and presumably binucleation/polyploidization,
382 function here in a coordinated biphasic manner. While considering solid tumors as non-healing wounds
383 [40], our observations, on the other hand, suggest that just wound healing by oval cells with
384 reprogramming potential represents the barrier mechanisms against cancer. This barrier, consisting of
385 adaptive, biphasic, and completed self-organization, is functionally efficient based on cell-cycle
386 checkpoint regulation coupled to the nuclear-cytoplasmic shuttle of the opposite regulators. The
387 transient activation of Myc found in centrosomes and cytoplasm but not in cell nuclei suggests that likely
388 N-Myc with its cell migration-promoting role [41, 42] rather than nuclear C-Myc that maintains stress-
389 dependent polyploidy linked to cancer-initiating pathways [43, 44] is functionally predominant in oval
390 cells, thereby restricting tumor growth and uncontrolled polyploidization. Perhaps, that is why the WB-
391 F433 cell line, relatively resistant to ionizing irradiation [15, 45], is not tumorigenic *in vivo* [14]. Further
392 research and clinical trials are needed to use the oval cells with therapeutic purposes, offering hope for
393 innovative and effective treatments for liver pathologies including cancer.

394 **Competing Interests**

395 The author(s) declared no potential conflicts of interest with respect to the research, authorship, and/or
396 publication of this article.

397 **Author Contributions**

398 All authors have contributed to this article as follows:

399 Conceptualization, J.E. and M.L.; methodology, J.E., M.L. and K.S.; writing-original draft preparation,
400 M.L.; writing-review and editing, J.E., B.G.; project administration, D.P.; funding acquisition, D.P.;
401 supervision, J.E. All authors gave final approval for the manuscript.

402 **References**

403 1. Higgins G, Anderson G. Experimental pathology of the liver restoration of the liver of the white
404 rat following partial surgical removal. Arch Pathol (Chic) 1931;12:186–202.

405 2. Devarbhavi H, Asrani SK, Arab JP, Nartey YA, Pose E, Kamath PS. Global burden of liver disease:
406 2023 update. J Hepatol. 2023;79(2):516-37.

407 3. Liu P, Mao Y, Xie Y, Wei J, Yao J. Stem cells for treatment of liver fibrosis/cirrhosis: clinical
408 progress and therapeutic potential. Stem Cell Res Ther. 2022;13(1):356.

409 4. Grisham JW, Porta EA. Origin and Fate of Proliferated Hepatic Ductal Cells in the Rat: Electron
410 Microscopic and Autoradiographic Studies. Exp Mol Pathol. 1964;3:242-61.

411 5. Fausto N. Liver regeneration. J Hepatol. 2000;32(1 Suppl):19-31.

412 6. Nguyen-Lefebvre AT, Selzner N, Wrana JL, Bhat M. The hippo pathway: A master regulator of
413 liver metabolism, regeneration, and disease. FASEB J. 2021;35(5):e21570.

414 7. Pefani DE, O'Neill E. Hippo pathway and protection of genome stability in response to DNA
415 damage. FEBS J. 2016;283(8):1392-403.

416 8. Zhang K, Zhang L, Liu W, Ma X, Cen J, Sun Z, et al. In Vitro Expansion of Primary Human
417 Hepatocytes with Efficient Liver Repopulation Capacity. Cell Stem Cell. 2018;23(6):806-19 e4.

418 9. Matsumoto T. Implications of Polyploidy and Ploidy Alterations in Hepatocytes in Liver Injuries
419 and Cancers. Int J Mol Sci. 2022;23(16).

420 10. Bird TG, Muller M, Boulter L, Vincent DF, Ridgway RA, Lopez-Guadamillas E, et al. TGFbeta
421 inhibition restores a regenerative response in acute liver injury by suppressing paracrine senescence.
422 Sci Transl Med. 2018;10(454).

423 11. Cheng N, Kim KH, Lau LF. Senescent hepatic stellate cells promote liver regeneration through IL-
424 6 and ligands of CXCR2. JCI Insight. 2022;7(14).

425 12. Chembazhi UV, Bangru S, Hernaez M, Kalsotra A. Cellular plasticity balances the metabolic and
426 proliferation dynamics of a regenerating liver. Genome Res. 2021;31(4):576-91.

427 13. Matsumoto T, Wakefield L, Tarlow BD, Grompe M. In Vivo Lineage Tracing of Polyploid
428 Hepatocytes Reveals Extensive Proliferation during Liver Regeneration. Cell Stem Cell. 2020;26(1):34-
429 47 e3.

430 14. Tsao MS, Smith JD, Nelson KG, Grisham JW. A diploid epithelial cell line from normal adult rat
431 liver with phenotypic properties of 'oval' cells. Exp Cell Res. 1984;154(1):38-52.

432 15. Gerashchenko BI, Salmina K, Krigerts J, Erenpreisa J, Babsky AM. Induced Polyploidy and Sorting
433 of Damaged DNA by Micronucleation in Radioresistant Rat Liver Epithelial Stem-Like Cells Exposed to X-
434 Rays. Probl Radiac Med Radiobiol. 2019;24:220-34.

435 16. Erenpreisa J, Freivalds T. Anisotropic staining of apurinic acid with toluidine blue.
436 Histochemistry. 1979;60(3):321-5.

437 17. Sugihara E, Kanai M, Matsui A, Onodera M, Schwab M, Miwa M. Enhanced expression of MYCN
438 leads to centrosome hyperamplification after DNA damage in neuroblastoma cells. Oncogene.
439 2004;23(4):1005-9.

440 18. Franklin JM, Ghosh RP, Shi Q, Reddick MP, Liphardt JT. Concerted localization-resets precede
441 YAP-dependent transcription. Nat Commun. 2020;11(1):4581.

442 19. Ma X, Qiu DK, Peng YS. Immunohistochemical study of hepatic oval cells in human chronic viral
443 hepatitis. World J Gastroenterol. 2001;7(2):238-42.

444 20. Shu W, Yang M, Yang J, Lin S, Wei X, Xu X. Cellular crosstalk during liver regeneration: unity in
445 diversity. Cell Commun Signal. 2022;20(1):117.

446 21. Zhang X, Neganova I, Przyborski S, Yang C, Cooke M, Atkinson SP, et al. A role for NANOG in G1
447 to S transition in human embryonic stem cells through direct binding of CDK6 and CDC25A. J Cell Biol.
448 2009;184(1):67-82.

449 22. Villacanas O, Perez JJ, Rubio-Martinez J. Structural analysis of the inhibition of Cdk4 and Cdk6
450 by p16(INK4a) through molecular dynamics simulations. J Biomol Struct Dyn. 2002;20(3):347-58.

451 23. Wolkenhauer O, Mesarovic M. Feedback dynamics and cell function: Why systems biology is
452 called Systems Biology. Mol Biosyst. 2005;1(1):14-6.

453 24. Wang L, Walker BL, Iannaccone S, Bhatt D, Kennedy PJ, Tse WT. Bistable switches control
454 memory and plasticity in cellular differentiation. Proc Natl Acad Sci U S A. 2009;106(16):6638-43.

455 25. Giuliani A, Bui TT, Helmy M, Selvarajoo K. Identifying toggle genes from transcriptome-wide
456 scatter: A new perspective for biological regulation. Genomics. 2022;114(1):215-28.

457 26. Erenpreisa J, Salmina K, Anatskaya O, Cragg MS. Paradoxes of cancer: Survival at the brink.
458 Semin Cancer Biol. 2022;81:119-31.

459 27. Noble R, Tasaki K, Noble PJ, Noble D. Biological Relativity Requires Circular Causality but Not
460 Symmetry of Causation: So, Where, What and When Are the Boundaries? Front Physiol. 2019;10:827.

461 28. Huang S, Ernberg I, Kauffman S. Cancer attractors: a systems view of tumors from a gene
462 network dynamics and developmental perspective. Semin Cell Dev Biol. 2009;20(7):869-76.

463 29. Gerashchenko BI, Salmina K, Eglitis J, Huna A, Grjunberga V, Erenpreisa J. Disentangling the
464 aneuploidy and senescence paradoxes: a study of triploid breast cancers non-responsive to
465 neoadjuvant therapy. Histochem Cell Biol. 2016;145(4):497-508.

466 30. Czarnecka-Herok J, Sliwinska MA, Herok M, Targonska A, Strzeszewska-Potyrala A, Bojko A, et
467 al. Therapy-Induced Senescent/Polyploid Cancer Cells Undergo Atypical Divisions Associated with
468 Altered Expression of Meiosis, Spermatogenesis and EMT Genes. Int J Mol Sci. 2022;23(15).

469 31. Mosteiro L, Pantoja C, de Martino A, Serrano M. Senescence promotes in vivo reprogramming
470 through p16(INK)(4a) and IL-6. Aging Cell. 2018;17(2).

471 32. Heng BC, Zhang X, Aubel D, Bai Y, Li X, Wei Y, et al. Role of YAP/TAZ in Cell Lineage Fate
472 Determination and Related Signaling Pathways. Front Cell Dev Biol. 2020;8:735.

473 33. Zhang S, Chen Q, Liu Q, Li Y, Sun X, Hong L, et al. Hippo Signaling Suppresses Cell Ploidy and
474 Tumorigenesis through Skp2. Cancer Cell. 2017;31(5):669-84 e7.

475 34. Allison DF, Wang GG. R-loops: formation, function, and relevance to cell stress. Cell Stress.
476 2019;3(2):38-46.

477 35. Lavado A, Park JY, Pare J, Finkelstein D, Pan H, Xu B, et al. The Hippo Pathway Prevents
478 YAP/TAZ-Driven Hypertranscription and Controls Neural Progenitor Number. Dev Cell. 2018;47(5):576-
479 91 e8.

480 36. So WK, Cheung TH. Molecular Regulation of Cellular Quiescence: A Perspective from Adult Stem
481 Cells and Its Niches. Methods Mol Biol. 2018;1686:1-25.

482 37. Mantel C, Guo Y, Lee MR, Kim MK, Han MK, Shibayama H, et al. Checkpoint-apoptosis
483 uncoupling in human and mouse embryonic stem cells: a source of karyotpic instability. Blood.
484 2007;109(10):4518-27.

485 38. Neganova I, Lako M. G1 to S phase cell cycle transition in somatic and embryonic stem cells. J
486 Anat. 2008;213(1):30-44.

487 39. Maya-Mendoza A, Moudry P, Merchut-Maya JM, Lee M, Strauss R, Bartek J. High speed of fork
488 progression induces DNA replication stress and genomic instability. Nature. 2018;559(7713):279-84.

489 40. Dvorak HF. Tumors: wounds that do not heal. Similarities between tumor stroma generation
490 and wound healing. N Engl J Med. 1986;315(26):1650-9.

491 41. Anderson S, Poudel KR, Roh-Johnson M, Brabletz T, Yu M, Borenstein-Auerbach N, et al. MYC-
492 nick promotes cell migration by inducing fascin expression and Cdc42 activation. Proc Natl Acad Sci U S
493 A. 2016;113(37):E5481-90.

494 42. Conacci-Sorrell M, Ngouenet C, Eisenman RN. Myc-nick: a cytoplasmic cleavage product of Myc
495 that promotes alpha-tubulin acetylation and cell differentiation. Cell. 2010;142(3):480-93.

496 43. Vazquez-Martin A, Anatskaya OV, Giuliani A, Erenpreisa J, Huang S, Salmina K, et al. Somatic
497 polyploidy is associated with the upregulation of c-MYC interacting genes and EMT-like signature.
498 Oncotarget. 2016;7(46):75235-60.

499 44. Anatskaya OV, Vinogradov AE. Polyploidy and Myc Proto-Oncogenes Promote Stress Adaptation
500 via Epigenetic Plasticity and Gene Regulatory Network Rewiring. Int J Mol Sci. 2022;23(17).

501 45. Gerashchenko BI, Azzam EI, Howell RW. Characterization of cell-cycle progression and growth
502 of WB-F344 normal rat liver epithelial cells following gamma-ray exposure. Cytometry A.
503 2004;61(2):134-41.

504